COMPUTER METHODS IN MATERIALS SCIENCE

2021, vol. 21, no. 3, 1–6
https://doi.org/10.7494/cmms.2021.3.0750

Conversion of compression test data into flow curve, accounting for barrelling

Shahin Khoddam*, Peter D. Hodgson

Deakin University, Institute for Frontier Materials, GTP Building, 75 Pigdons Road, Waurn Ponds, VIC 3216, Australia.

Abstract

Current solutions to convert the axis-symmetric compression test (ACT) data to flow data ignore the barrelling deformation in the sample. This work presents a solution for the test which accounts for the sample's barrelling by discretising it into a finite number of layers of different radii. The solution assumes a constant and sliding friction at the anvil-sample interface. The sample's flow behaviour is identified by combining a recent kinematic solution of the test, Prandtl–Reuss–Mises's equations and a slab-analysis of the layers. It also involves an averaging of the effective plastic stresses developed in the individual layers. The solution is verified for a special case of no-barrelling which matches the currently used solution.

Keywords: Compression test; flow curve identification; barrelling induced shear; multi-layer; slab analysis

1. Introduction

The axis-symmetric compression test (ACT) is the most commonly used physical simulation to characterize the hot flow behaviour of materials and their associated strength-deformation related phenomena such as phase changes (Madej et al., 2008; Rauch et al., 2017) and material recovery (e.g. SRX (Khoddam & Hodgson, 2015), DRX (Guerrero et al., 2012) etc.). Despite a large number of works in the last 80 years to find detailed solutions for the test (see for example Osakada, 2010), only simplified solutions of the test are available. This is partly due to the complex nature of this boundary value problem and its transient boundary conditions which include factors such as friction (Gzyl et al., 2015; Khoddam et al., 2021), barrelling (Khoddam et al., 2019), foldover and the thermal boundary conditions (Khoddam et al., 2011).

A full physical simulation and description of the material deformation based on the ACT, requires both detailed solutions for deformation (e.g. effective strain and strain rate) and the required forces (e.g. effective stress) in the deforming sample. While there exist a few kinematic solutions of the ACT which account for barrelling (e.g. Avitzur, 1968; Khoddam 2018), the available flow stress solutions of the test (e.g. Avitzur, 1968; Rowe, 1979) fail to account for the sample's profile changes and are only based on a cylindrical deformed profile.

The advent of numerical methods, as a powerful analytical tool, has enabled scientists and engineers to solve complex problems in a detailed and coupled fashion significantly beyond the limits of the closed-form counterpart solutions (Rauch et al., 2007). Examples of these are numerical methods applied to many parameter estimation problems (Beck & Arnold, 1977) and inverse problems.

* Corresponding author: shahin@deakin.edu.au
ORCID ID's: 0000-0002-5205-2086 (S. Khoddam), 0000-0002-6985-1319 (P.D. Hodgson)

1.1. Numerical or closed-form solution?

The might of numerical modelling and solutions has found far few practical applications for material flow characterization. The limited and cautious use of numerical flow identification methods compared to their closed-form counterparts has two main reasons: 1. they require sophisticated platforms such as special subroutines to be performed under a commercially available software or a dedicated in-house numerical code which makes them unpopular, 2. the optimisation-based numerical solutions obtained by such approaches are prone to entrapment in a local minimum (Petitprez & Mocellin, 2013; Sztangret et al., 2014). Therefore, numerical methods are not currently a viable replacement for the closed form solution of the mechanical tests, including ACT.

A commonly used closed-form solution for ACT, proposed by Avitzur (1968), which assumes a constant and sliding friction is:

$$\sigma_0 = \frac{L}{\pi \bar{R}^2 \left(1 + \frac{2m}{3\sqrt{3}H}\bar{R}\right)} \tag{1}$$

where σ_0, $\bar{R}$, m, H and L are flow stress, sample's equivalent radius, friction factor and deformation load, respectively. In this solution, the deformed profile is represented by a cylindrical surface of effective radius of $\bar{R} = 0.5D_0\sqrt{(H_0/H)}$ which is assumed constant across the sample's axis. D_0, H_0 and H are the samples undeformed diameter, height and deformed height, respectively (see Figure 1).

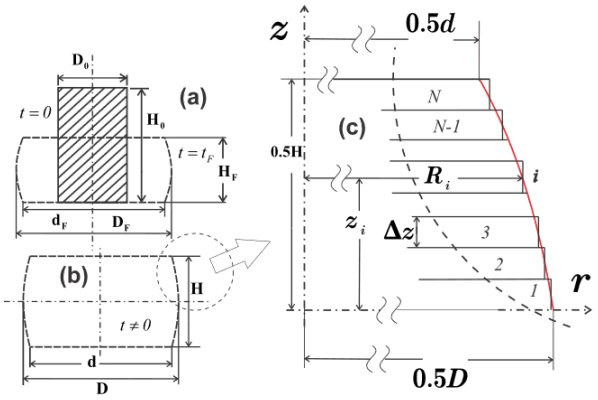

Fig. 1. Schematic of specimen geometry, its real, quadratic and multi-layered profiles and illustration of symbols: a) Initial geometry (t = 0) and final geometry ($t = t_F$); b) geometry at an arbitrary time slice $t \neq 0$, sample's real barrelled profile; c) an inset of (b) discretised in a multi-layer fashion; the quadratic profile (shown with red line) and multi-layer layer are overlaid

In this work we aim to reduce the limitation of the existing closed-form solution of ACT to address the shear deformation in the sample. This is expected to improve the accuracy of the flow behaviour characterization.

The next section defines some terms in preparation for the detailed solution of the test to be presented in this work.

2. Definition of the terms

The barrelled sample, its polar coordinate system and the symbols which represent the deformation parameters are shown in Figure 1. The representation highlights the shear induced barrelling of the sample which is currently ignored in the commonly used theory of axisymmetric compression flow stress conversion.

2.1. The virtual quadratic profile

Figure 1 shows a barrelled sample represented with three profiles; (a) and (b) typical real undeformed and deformed profiles and (c) an overlay of the virtual quadratic profile and its multi-layer discretisation.

The virtual quadratic profile, shown using a dashed red line in Figure 1, is a second-order curve which represents the variation of the sample's radius as a quadratic function of z. Its radius, $R(z)$ varies from $0.5D$ in the sample's mid-plane to $0.5d$ at the sample's top-plane; The profile radius $R(z)$ as a function of z, the layer number i and the total number of layers N is expressed as:

$$R(z) = 0.5D - \frac{2(D-d)z^2}{H^2} = R_i = 0.5D - \frac{(D-d)i^2}{2N^2} \tag{2}$$

2.2. Limitations in currently available ACT data

Currently available ACT test rigs only provide $L - H$ data which hinder the barrelling investigations. The flow identification solution developed in this work, requires an experimental setup which can measure $L - H - D - d$ data. In the sequel, we explain that how the proposed quadratic profile can facilitate the collection of such data in the test rigs of future.

Concurrent measurement of $D - H$ data during the test is much easier than that of $d - H$. Therefore, a quadratic profile and the incompressibility principle of the sample's have been used (Fardi et al., 2017) to

correlate the barrelled sample's initial geometry with the barrelling data including the mid-plane and top-plane deformed diameters D and d. Thus, one only needs to measure the initial geometry (H_0 and D_0) and D to estimate the top-plane diameter d using the following correlation:

$$d = \frac{\sqrt{5}\sqrt{H(9D_0^2H_0 - 4D^2H) - 2DH}}{3H} \tag{3}$$

2.3. Multi-layer formulation of the barrelling

It can be seen in Figure 1 that the sample's outside radius $R_0 = R_i$ varies from $0.5D$ at the first layer ($i = 1$) to $0.5d$ at the last layer ($i = N$). For simplicity, only the upper half of the sample has been discretised along the sample's axis of symmetry, z:

$$\Delta z = \frac{H}{2N} \tag{4}$$

$$z = i\Delta z = \frac{iH}{2N} \tag{5}$$

Before presenting the stress analysis in the multi-layer formulation, a short summary of and recent kinematic analysis (Khoddam, 2018) will be presented. The kinematic model will be used to find a stress-strain relationship in the deforming sample.

3. Velocity fields

A kinematically admissible velocity field for ACT was proposed by Khoddam (2018) to account for the barrelling:

$$\dot{u}(r,z) = r\dot{H}\left(B + 2\frac{(1-2BH)}{H^2}z\right) \tag{6}$$

$$\dot{v}(z) = 2\dot{H}z\frac{(BH(2z-H)-z)}{H^2} \quad (0 \le z \le 0.5H) \tag{7}$$

$$\dot{v}(z) = \frac{2\dot{H}z((BH(-H-2z)+z))}{H^2} \quad (0 \le z \le -0.5H) \tag{8}$$

where u and v denote the magnitude of the radial and axial components of displacements for a material point in the deforming sample and $\dot{u}$ and $\dot{v}$ are the corresponding velocity components of the point. The velocity field model given by Equations (6) to (8), also known as the Exponential Profile Model (EPM), comprises two non-zero velocity components, $\dot{u}$ and $\dot{v}$ and incorporates a barrelling parameter B to link the components. The parameter was also used to enforce their admissibility and compliance with the incompressibility principle.

3.1. Stress-strain rate relationship

EPM's strain rate equations were expressed as (Khoddam, 2018):

$$\dot{\varepsilon}_{zz} = \frac{\partial \dot{v}}{\partial z} = -2\dot{H}\frac{(BH(H-4z)+2z)}{H^2} \quad 0 \le z \le 0.5H \tag{9}$$

$$\dot{\varepsilon}_{rr} = \frac{\partial \dot{u}}{\partial r} = \dot{H}\left(B - \frac{6(1+2BH)z^2}{H^3}\right) \tag{10}$$

$$\dot{\varepsilon}_{\theta\theta} = \frac{\dot{u}}{r} = \dot{H}\left(B - \frac{6(1+2BH)z^2}{H^3}\right) \tag{11}$$

In addition, shearing components of the strain rate in the sample can be found as:

$$\dot{\varepsilon}_{rz} = \frac{1}{2}\left(\frac{\partial \dot{u}}{\partial z} + \frac{\partial \dot{v}}{\partial r}\right) = \dot{H}\frac{(1-2BH)r}{H^2} \tag{12}$$

$$\dot{\varepsilon}_{r\theta} = \dot{\varepsilon}_{z\theta} = 0 \tag{13}$$

3.2. Plastic stress-strain rate relationship

From Prandtl–Reuss–Mises' stress-strain rate law (Prandtl, 1924; Reuss, 1930) (ignoring the elastic deformation):

$$\dot{\varepsilon}_{ij} = \dot{\lambda}\sigma'_{ij}, \quad \dot{\lambda} = \frac{\dot{\varepsilon}_{rr}}{\sigma'_{rr}} = \frac{\dot{\varepsilon}_{zz}}{\sigma'_{zz}} = \frac{\dot{\varepsilon}_{\theta\theta}}{\sigma'_{\theta\theta}} = \frac{\dot{\varepsilon}_{rz}}{\sigma'_{rz}} = \frac{\dot{\varepsilon}_{r\theta}}{\sigma'_{r\theta}} = \frac{\dot{\varepsilon}_{z\theta}}{\sigma'_{z\theta}} \tag{14}$$

In Equation (14), the deviatoric stress tensor, σ'_{ij}, is found by subtracting the hydrostatic stress tensor, σ_m, from the Cauchy stress tensor, σ_{ij}:

$$\sigma'_{ij} = \sigma_{ij} - \frac{\sigma_{kk}}{3}\delta_{ij} = \sigma_{ij} - \sigma_m\delta_{ij} \tag{15}$$

where the Kronecker delta $\sigma_{ij} = 0$ when $i \neq j$ and $\sigma_{ij} = 1$ when $i = j$.

Assuming $\sigma_{rr} = \sigma_{\theta\theta} = \sigma$, $\sigma_{r\theta} = \sigma_{z\theta} = 0$ and $\sigma_{zz} = -p = p(r)$, the hydrostatic stress becomes:

$$\sigma_m = \frac{\sigma_{kk}}{3} = \frac{1}{3}(2\sigma_{rr} - p) = \frac{1}{3}(2\sigma - p) \tag{16}$$

Combining Equations (15) and (16) gives:

$$\sigma'_{rr} = \sigma'_{\theta\theta} = \frac{1}{3}(\sigma + p) \tag{17}$$

and

$$\sigma'_{zz} = -\frac{2}{3}(\sigma + p) \tag{18}$$

Combining equations (14), (17) and (18) and solving Equation (14) simultaneously leads to:

$$\sigma'_{rz} = \sigma_{rz} = 0 \tag{19}$$

and

$$\sigma_{rr} = \sigma_{\theta\theta} = \sigma = -p(r) \tag{20}$$

Equations (19) and (20) enable us to construct a free body diagram of the forces in a typical layer shown in Figure 1.

4. Free body diagram of a slab element

The frictional shear stress results in an external friction force at the anvil-sample interface. Isolating the shown element in Figure 2 from the rest of the deforming domain, one has to expose the corresponding internal force induced by frictional shear stress in each layer at its interface with the rest of the continuum. The exposure acts as an external force (or external shearing stress) in the free body diagram; Figure 2: τ_f shown on the top and lower surfaces of the differential element. We note that τ_f is only a share (fraction) of the total shearing stress τ'_f at the anvil-slice interface. A correlation of τ_f with τ'_f will be proposed later in this work.

Given the non-zero nature of $\sigma_{rr} = \sigma_{\theta\theta} = -p(r)$, the radial growth of σ_{rr} ($\sigma_{rr} = (\partial\sigma_{rr}/\partial r)dr$) has been included in the differential element in Figure 2.

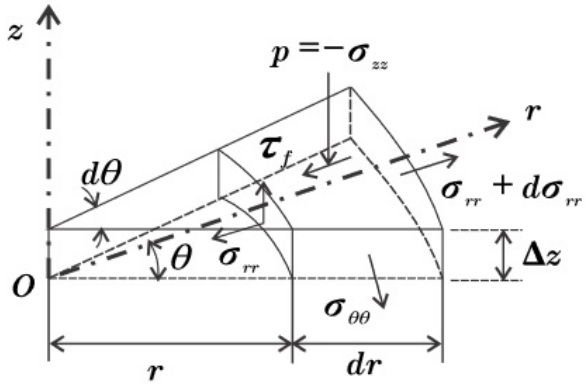

Fig. 2. A differential element of the specimen for a typical layer

The elementary slice of the barrelled disc, shown in Figure 2, is bounded on its top and bottom sides by two radial planes that pass through the axis of symmetry. They are also bounded tangentially by an angle $d\theta$ and are radially bounded by two concentric cylinders of radii of r and $r + dr$. The element represents a layer which at its upper (or lower) surface retains the top (or bottom) surface of the disc which is in contact with the anvils. Given $\sigma_{rz} = 0$ in the sample, the same element represents also a typical layer which is not necessarily in contact with the anvil.

From the equilibrium of the forces arising from different stress components at each side of the element, the free body diagram of the slice can be constructed, simplified and solved. The radial equilibrium of the forces in the shown free body diagram becomes:

$$\Delta z\sigma_{rr} r d\theta - \Delta z\left(\sigma_{rr} + \frac{\partial\sigma_{rr}}{\partial r}dr\right)(r + dr)d\theta + 2\tau_f r d\theta dr + \frac{2\sigma_{\theta\theta} dr\Delta z d\theta}{2} = 0 \tag{21}$$

Dividing both sides by $dRd\theta$, omitting differential products of orders above one, applying $-\Delta z\sigma_{rr} + \sigma_{\theta\theta}\Delta z = 0$ and dividing both sides by r, Equation (21) reduces to:

$$-\Delta z\sigma_{rr} + 2\tau_f dr = 0 \tag{22}$$

Let us consider a specimen that is only composed of one layer. Consequently, the total frictional shearing stress is represented as τ'_f. Assuming a constant friction factor m at the anvil-specimen interface, the total frictional shearing stress τ'_f can be estimated as:

$$\tau'_f = m\frac{\sigma_0}{\sqrt{3}} \quad 2N = 1 \tag{23}$$

We assume a laminar deformation energy consumption in a multi-layer sample in which the frictional shearing stress on a layer τ_f is reversely proportional to the total number of the layers N and directly proportional to τ'_f. Combining this assumption and Equation (23):

$$\tau_f = \frac{1}{2N}\tau'_f = \frac{m\sigma_0}{2N\sqrt{3}} \tag{24}$$

The assumption can be justified by noting that τ'_f represents the energy needed to deform the entire sample while τ_f is responsible to deform only one layer of a multi-layer sample. Therefore, Equation (22) can be written in a unified form for all elements as:

$$-\Delta z d\sigma_{rr} + \frac{m\sigma_0}{N\sqrt{3}}dr = 0 \tag{25}$$

Given $d\sigma_{rr} = -dp$, therefore:

$$dp = -\frac{m}{N\sqrt{3}\Delta z}\sigma_0 dr \tag{26}$$

The solution is:

$$p(r) = -\frac{m}{N\sqrt{3}\Delta z}\sigma_0 r + C \tag{27}$$

Substituting $N\Delta z = 0.5H$ and applying the boundary condition: $R = R_i$, $p = \sigma_0$:

$$C = \sigma_0\left(1+\frac{2m}{\sqrt{3}H}R_i\right) \tag{28}$$

Therefore:

$$p = p(r) = \sigma_0\left(1+\frac{2m}{\sqrt{3}H}\left(1-\frac{R}{R_i}\right)R_i\right) \tag{29}$$

It can be seen from the above that the maximum pressure occurs at $R = 0$:

$$p_{\max} = \sigma_0\left(1+\frac{2m}{\sqrt{3}H}R_i\right) \tag{30}$$

The average pressure becomes:

$$p_{ave} = \frac{2\pi\int_{R=0}^{R_0=R_i} Rp(r)dR}{\pi R_i^2} = \sigma_0\left(1+\frac{2m}{3\sqrt{3}H}R_i\right) \tag{31}$$

Finally, p_{ave} in the top layer ($i = N$) is expressed in terms of the load L which is required to deform the layer as:

$$L = \pi R_i^2 p_{ave} \tag{32}$$

load L applied by anvil to plastically deform the sample remains unchanged for all layers ($L = L_i$).

Similarly, it can be shown that for all other layers, the same expressions for average pressure and load are applicable; the only difference for different layers is their different outer radius. The layer outer radius R_i grows from $0.5d$ at the top layer ($i = N$) to $0.5D$ at the lower layer ($i = 1$).

The solution for all layers can be expressed in a unified multi-layer fashion as follows:

$$R(z) = R_i = 0.5D - \frac{2(D-d)z^2}{H^2} = 0.5D - \frac{(D-d)i^2}{2N^2} \qquad (i = 1, ..., N) \tag{33}$$

and:

$$L = L_i = \pi R_i^2\sigma_0\left(1+\frac{2m}{3\sqrt{3}H}R_i\right) \quad (i = 1, ..., N) \tag{34}$$

5. Flow stress averaging

To account for barrelling in the sample, we propose to use an averaging scheme to account for the barrelled geometry when the ACT test data are converted to the flow stress. Let's apply Equation (33) for each layer and add both sides of the resulted equations for $i = 1$ to $i = N$, so the sum can be written as:

$$NL = \sum_{i=1}^{N}\pi R_i^2\sigma_0\left(1+\frac{2m}{3\sqrt{3}H}R_i\right) \tag{35}$$

Therefore, the average flow stress becomes:

$$\sigma_0 = \frac{NL}{\sum_{i=1}^{N}\pi R_i^2\sigma_0\left(1+\frac{2m}{3\sqrt{3}H}R_i\right)} \tag{36}$$

The above equation can be verified for a special case in which the barrelling does not occur; it can be easily shown that for a special case of zero barrelling ($R_i = \bar{R}$), the above equation reduces to the slab method formula (Eq. (1)):

$$\sigma_0 = \frac{NL}{N\pi\bar{R}^2\left(1+\frac{2m}{3\sqrt{3}H}\bar{R}\right)} = \frac{L}{\pi\bar{R}^2\left(1+\frac{2m}{3\sqrt{3}H}\bar{R}\right)} \tag{37}$$

6. Effective strain rate and strain averaging

The existing solutions of ACT assume a homogeneous effective plastic strain rate of the following form in the sample:

$$\dot{\bar{\varepsilon}} = \frac{\dot{H}}{H} \tag{38}$$

and their homogeneous effective strain can be estimated as:

$$\bar{\varepsilon} = \frac{-1}{H}\int_{H_0}^{H}\dot{\bar{\varepsilon}}dH = -1\int_{H_0}^{H}\frac{dH}{H} = \ln H_0 - \ln H \tag{39}$$

Alternatively, the interested reader may want to estimate the effective non-homogeneous strain rate and strain and their distributions in the sample using the EPM model (Khoddam, 2018).

7. Discussions and conclusion

Based on the multi-layer solution presented in this work, one can easily reduce the ACT data to flow stress data.

The conversion approach accounts for the shear induced barrelling in a convenient way using the following steps:

– First, the sample is divided into a finite number of layers and an average flow stress is calculated; the inputs are $L - H - D$ data, number of layers N (to be chosen), and the friction factor m. The top-plane diameter d is found using Equation (3).
– Next, the radii of each layer in the discretised sample are found using Equation (33). These will be used in Equation (36) to find the average flow stress in the barrelled sample.

While the solution presented in this work presents an average and homogeneous estimate for the sample's flow stress, its corresponding effective strain rate and strain could be either estimated as homogeneous values using equations (38) and (39) or as non-homogeneous values following the EPM's steps (Khoddam, 2018).

The solution was verified for a special case with sliding friction at the anvil-sample interface and a constant friction factor. The case involved a non-barrelled sample. The special case solution complied fully with the commonly used slab solution of the ACT test.

References

Avitzur, B. (1968). *Metal forming. Processes and analysis*. McGraw-Hill.

Beck, J.V., & Arnold, K.J. (1977). *Parameter Estimation in Engineering and Science*. John Wiley & Sons.

Fardi, M., Abraham, R., Hodgson, P.D., & Khoddam, S. (2017). A New Horizon for Barrelling Compression Test: Exponential Profile Modelling. *Journal of Advanced Materials*, *19*(11), 1700328, https://doi.org/10.1002/adem.201700328.

Guerrero, G.A., Granados, I.M., & Marrero J.M.C. (2012). Determination of the critical parameters for the onset of dynamic recrystallization (DRX) in advanced ultrahigh strength steels (A-UHSS) microalloyed with boron. *Computer Methods in Materials Science*, *12*(3), 152–162.

Gzyl, M.Z., Sikora, K., Olejnik, L., Rosochowski, A., & Qarni, M.J. (2015). Determination of friction factor by ring compression testing and FE analysis. *Computer Methods in Materials Science*, *15*(1), 156–161.

Khoddam, S. (2018). Deformation under combined compression and shear: a new kinematic solution. *Journal of Materials Science*, *54*(6), 4754–4765. https://doi.org/10.1007/s10853-018-03201-0.

Khoddam, S., & Hodgson, P.D. (2015). The need to revise the current methods to measure and assess static recrystallization behavior. *Mechanics of Materials*, *89*, 85–97. http://dx.doi.org/10.1016/j.mechmat.2015.06.008.

Khoddam, S., Hodgson, P.D. & Bahramabadi, M.J. (2011). An inverse thermal-mechanical analysis of the hot torsion test for calibrating the constitutive parameters. *Materials & Design*, *32*(4), 1903–1909. https://doi.org/10.1016/j.matdes.2010.12.010.

Khoddam, S., Solhjoo, S. & Hodgson, P.D. (2019). A power-based approach to assess the barrelling test's weak solution. *International Journal of Mechanical Sciences*, *161–162*, 105033. https://doi.org/10.1016/j.ijmecsci.2019.105033.

Khoddam, S., Fardi, M. & Solhjoo, S. (2021). A verified solution of friction factor in compression test based on its sample's shape changes. International Journal of Mechechanical Science, 193, 106175. https://doi.org/10.1016/j.ijmecsci.2020.106175.

Madej, Ł., Mrozek, A., Kuś, W., Burczyński, T., & Pietrzyk, M. (2008). Concurrent and upscaling methods in multi scale modelling – case studies. *Computer Methods in Materials Science*, *8*(1), 1–15.

Osakada, K. (2010). History of plasticity and metal forming analysis. *Journal of Materials Processing Technology*, *210*(11), 1436–1454.

Petitprez, M., & Mocellin, K. (2013). Non standard samples behaviour law parameters determination by inverse analysis. *Computer Methods in Materials Science*, *13*(1), 56–62.

Prandtl, L. (1924). Spannungsverteilung in plastischen Körpern. In *Proceedigs of the first International Conference on Applied Mechanics, Delft University* (pp. 43–54).

Rauch, L., Madej, L., Jurczyk, T., & Pietrzyk, M. (2007). Complex Modelling Platform based on Digital Material Representation. In G. Loureiro & R. Curran (Eds.), *Complex Systems Concurrent Engineering* (pp. 403–410). Springer-Verlag London

Rauch, Ł., Skóra, M., Bzowski, K., & Pietrzyk M. (2017). Numerical model of cold deformation of TRIP steel. *Computer Methods in Materials Science*, *17*(4), 207–217.

Reuss, A. (1930). Berücksichtigung der elastischen Formänderung in der Plastizitätstheorie. *ZAMM – Journal of Applied Mathematics and Mechanics / Zeitschrift für Angewandte Mathematik und Mechanik*, *10*(3), 266–274.

Rowe, G.W. (1979). *Elements of metalworking theory*. E. Arnold.

Sztangret, Ł., Sztangret, M., Kusiak, J. & Pietrzyk, M. (2014). Metamodel of the plane strain compression test as a replacement of FE model in the inverse analysis. *Computer Methods in Materials Science*, *14*(4), 215–227.